Nanoscale

PAPER

View Article Online
View Journal | View Issue

Cite this: *Nanoscale*, 2024, **16**, 21340

High-throughput screening of bifunctional catalysts for oxygen evolution/reduction reaction at the subnanometer regime†

Rahul Kumar Sharma, Harpriya Minhas and Biswarup Pathak *

The development of low-cost, stable, and highly efficient electrocatalysts for the bifunctional oxygen evolution reaction (OER) and oxygen reduction reaction (ORR) is crucial for advancing future renewable technologies. In this study, we systematically investigated the OER and ORR performance of subnano clusters across the 3d, 4d, and 5d transition metal (TM) series of varying sizes using first-principles calculations. The fluxional identity of these clusters in the subnanometer regime is reflected in their non-monotonic catalytic activity. We established a size-dependent scaling relationship between OER/ORR intermediates, leading to a reshaping of the activity volcano plot at the subnanometer scale. Our detailed mechanistic investigation revealed a shift in the apex of the activity volcano from the Pt(111) and IrO_2 surfaces to the Au_{11} clusters for both OER and ORR. Late transition metal subnano clusters, specifically Au_{11}, emerged as the best bifunctional electrocatalyst, demonstrating significantly lower overpotential values. Furthermore, we categorized our catalysts into three clusters and employed the Random Forest Regression method to evaluate the impact of non-*ab initio* electronic features on OER and ORR activities. Interestingly, d-band filling emerged as the primary contributor to the bifunctional activity of the subnano clusters. This work not only provides a comprehensive view of OER and ORR activities but also presents a new pathway for designing and discovering highly efficient bifunctional catalysts.

Received 5th July 2024,
Accepted 27th October 2024

DOI: 10.1039/d4nr02787f

rsc.li/nanoscale

1. Introduction

Developing sustainable and green technologies for efficient energy conversion is essential to meet the growing energy demands and ensure a secure, sustainable future.[1,2] In this context, electrochemical energy conversion technology is the most promising technology, with applications in metal–air batteries, hydrogen-producing devices, and fuel cells.[3–5] Notably, catalysts play a crucial role in these devices, facilitating a series of complex multistep reactions at the different electrodes. For instance, the oxygen evolution reaction (OER) and oxygen reduction reaction (ORR) are two core reactions in these energy storage devices that occur at the anode and cathode, respectively, determining the electrochemical reaction rates of these devices.[6,7] However, these electrode reactions typically exhibit high overpotential values and sluggish kinetics owing to the multi-electron transfer process, which impedes their widespread commercialization.[8,9] Therefore, developing suitable catalysts with high activity is essential for the practical application of energy-related devices. Currently, state-of-the-art electrocatalysts for OER and ORR primarily rely on precious metals such as Pt and IrO_2.[10–12] However, these precious metals' scarcity, low selectivity, and high costs restrict their large-scale application, motivating researchers to develop low-cost electrocatalysts with excellent activity and stability under electrochemical conditions.[13–15] In particular, designing efficient bifunctional electrocatalysts that facilitate both the OER and ORR in the same electrolyte is indispensable for the rapid development of regenerative fuel cells.

Due to their unique electronic and structural properties, subnano clusters have emerged as an important class of electrocatalysts in heterogeneous catalysis.[16] At finite temperatures, these molecular units possess a relatively flat potential energy surface (PES), leading to dynamic and non-Arrhenius behavior.[17] Additionally, their multiple under-coordinated sites result in a fluxional identity, causing a non-monotonic catalytic activity relative to cluster size and element. Previously, Zandkarimi *et al.* demonstrated a breaking of the scaling relationship for ORR at the subnanometer regime, attributed to the fluxionality of bare and graphene-supported Pt_n clusters (n = 1–6).[18] Similarly, our group has also reported significant variations in ORR activity of graphene-supported $Pt_{7,8}$ subnano clusters compared to their bulk counterparts.[19] Additionally, theoretical investigations have focused on the computational

Department of Chemistry, Indian Institute of Technology Indore, Indore 453552, India. E-mail: biswarup@iiti.ac.in

†Electronic supplementary information (ESI) available: Computational details, scaling relationships, reaction energy diagrams, and Pearson correlation coefficient plots. See DOI: https://doi.org/10.1039/d4nr02787f

screening of trimetallic clusters for OER and ORR.[20] Recently, Zhang *et al.* observed a shift in the apex of the volcano peak from Pt to Au with transition metal (TM_n) clusters (M = Pt, Pd, Au, and Ag, n = 1–6) for ORR.[21] Despite the significance of these findings, a systematic exploration of high-performance subnanometer TM_n clusters with varying elemental compositions and sizes is still lacking. Furthermore, the development of active bifunctional catalysts and the correlation between their catalytic activity and electronic descriptors of clusters in the subnanometer regime remain elusive.

In this work, we focus on screening bifunctional electrocatalysts for the OER and ORR in the subnanometer regime using density functional theory (DFT). We characterized the fluxional identity of the subnano catalysts by systematically investigating the adsorption energy characteristics across 3d, 4d, and 5d transition metal clusters (TM_n), where n = 7–15. The size-dependent scaling relationship between the adsorption energies indicates that the catalytic activity of subnano clusters significantly differs from their bulk counterparts. Furthermore, our systematic exploration of the four-electron OER and ORR mechanism in an acidic medium reveals a shift in the apex of the activity volcano plots for OER/ORR activity. Further, to understand the origins of bifunctional activity, we categorized the clusters into three groups and analyzed the impact of the electronic properties of the local chemical environment on the OER/ORR activity. Our study screens potential bifunctional catalysts and establishes a correlation between electronic properties and catalytic activities of subnano clusters, providing valuable guidance for designing efficient catalysts for OER and ORR activities (Scheme 1).

2. Results and discussion

2.1. Adsorption characteristics of OER/ORR intermediates

To understand the OER/ORR activity of the subnano clusters, we analyzed the adsorption characteristics of the principal intermediates (*O, *OH, and *OOH) within the subnanometer regime. Identifying the most stable geometries and adsorption positions for these intermediates is challenging owing to the diverse distribution and vast chemical space of subnano clusters. To address this, we extracted the previously reported optimized global minima (GM) geometries for 3d, 4d, and 5d transition metal subnano clusters, denoted as TM_n (where n = 7–15).[22] Tc and La were excluded from our investigation due to their radioactivity and toxicity.[23] TM_n clusters in this size

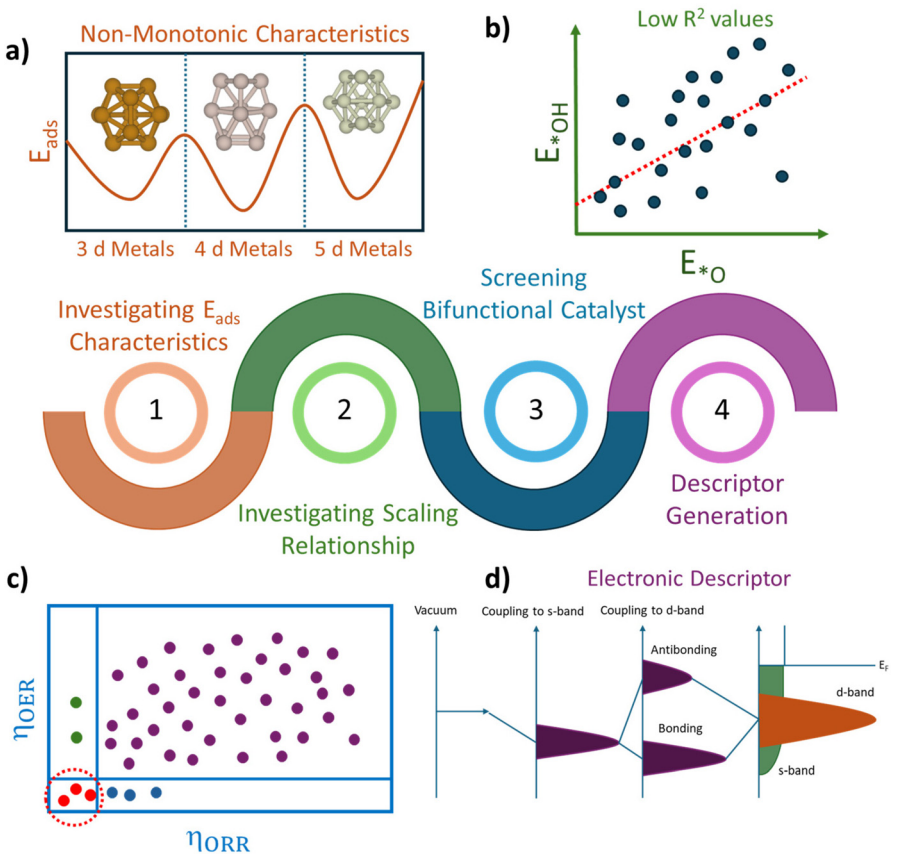

Scheme 1 Schematic illustration of our DFT framework for screening active bifunctional electrocatalysts for OER/ORR activity in the subnanometer regime. The four streamlined processes include (a) investigating adsorption energies (E_{ads}) of principal OER/ORR intermediates across different transition metal subnano clusters of varying sizes (TM_n), (b) investigating the scaling relation between OER/ORR intermediates, (c) screening active bifunctional catalysts, and (d) deriving a correlation between electronic descriptors and OER/ORR activity.

regime predominantly exhibit non-bulk-like facets, with diverse coordination environments and electronic properties, distinguishing them from bulk counterparts like the Pt (111) surface. Unlike the highly symmetric configurations of larger TM_n clusters (n = 38, 55, 79),[24,25] their stable geometries show extensive structural diversity, including non-planar, planar, pentagonal bipyramidal, Mackay icosahedral, distorted icosahedral, pentagonal antiprism, and capped square or triangular bipyramids, among others. The irregular facets provide both saturated (highly coordinated) and unsaturated (low-coordinated) sites, contributing to fluxional behavior and disrupting conventional scaling relationships due to varying binding affinities.[18] These structural variations lead to a non-monotonic change in catalytic activity with size and composition, offering opportunities to reshape conventional ORR volcano plots.

Given the fluxionality of subnano clusters, resulting from multiple heterogeneous sites, we optimized multiple geometries of the single-intermediate adsorbed onto different active sites (top and bridge) of the clusters (>2000 configurations). Subsequently, using the Bell–Evans–Polanyi (BEP) principle, which states that a lower activation energy accompanies the most stable adsorption energy (E_a),[26,27] we have extracted the most stable configurations for the further investigation of the OER/ORR reaction mechanism. Notably, 3-fold hollow positions are unstable adsorption sites for OER/ORR intermediates at the subnanometer regime and were excluded from our investigation.[19,28] All calculations were performed for optimization using density functional theory (DFT) with the Vienna *ab initio* simulation (VASP) package.[29] A detailed description of the computational method is provided in Text S1, ESI.† The adsorption energy of each intermediate (E_{ads}) on the TM_n is computed as follows:

$$E_{ads} = E(TM_nX) - E(TM_n) - E(X) \quad (1)$$

where $E(TM_nX)$ is the energy of the intermediate adsorbed geometry of the different TM_n clusters, $E(TM_n)$ is the energy of the bare clusters, and $E(X)$ is the energy of the intermediate in the gas phase.

The size-specific values of E_{ads} for *O, *OH and *OOH intermediates across the different TM series are summarized in Fig. 1. The non-monotonic distribution of E_{*O}, E_{*OH}, and E_{*OOH} represents the fluxional behavior of the subnano clusters, contributing to their variable OER/ORR activity; however, a periodic pattern is observed for each intermediate across different TM series (Fig. 1). Specifically, E_{*O}, E_{*OH}, and E_{*OOH} generally decrease upon transition from v^1 (metals with one valence electron in the d-orbitals) to v^{10}, indicating that strong electronic repulsion weakens the coupling between the cluster and the intermediates. Compared to the bulk Pt (111) surface and Pt_{79} nanoclusters,[25] the majority of the subnano clusters exhibited a shift towards more negative E_{ads}, indicative of stronger binding affinities due to their under-coordinated sites, except for TM_n clusters with v^{10} configurations. The highest E_{ads} are observed for Ta_{13} (−7.96 eV for E_{*O}), Mn_{11} (−5.69 eV for E_{*OH}), and Cr_{12} (−4.41 eV for E_{*OOH}), while the lowest are found for Hg_{13} (−1.09 eV for E_{*O}), Hg_8 (−1.04 eV for E_{*OH}), and Hg_{14} (+0.03 eV for E_{*OOH}). These extremes represent a non-Sabatier range, where catalysts with very strong or weak E_{ads} may lead to either poisoning or physisorption, thus reducing the overall catalytic activity. Overall, the distribution of E_{ads} in the subnanometer regime demonstrates a strong dependence on the valence electrons in the d-orbitals.

2.2. Analyzing scaling relationship at subnanometer regime

Scaling relationships are simple linear correlations between the thermodynamic properties of intermediates across different surfaces. However, these relationships impose intrinsic limitations on the maximum activity of the catalyst. Zandkarimi *et al.* previously demonstrated the breaking of the conventional scaling relationship between the ORR intermediates, attributed to the isomeric diversity and fluxional behavior of subnano clusters.[18] Similarly, in our study, we examined the correlation between OER/ORR for our subnano catalysts, as depicted in Fig. 2.

From Fig. 2, it is evident that the scaling relationship in the non-scalable regime is size-dependent across different TM series, with TM_7 and TM_{12} representing the highest and lowest values of the coefficient of determination (R^2 = 0.91 and 0.60 for E_{*O} *vs.* E_{*OH}, respectively). Observing the overall distribution (Fig. S1†), we note a scaling relationship for subnano clusters with R^2 = 0.84 and 0.88 (compared to R^2 = 0.91 for bulk surfaces)[18] between E_{*O} *vs.* E_{*OH} and E_{*OH} *vs.* E_{*OOH} intermediates, respectively. The variable correlation across different sizes could be attributed to differences in the adsorption sites and changes in the electronic structure, resulting in varying E_{ads} across different surfaces. In the investigation of scaling relationship, the slope of the best-fit line indicates the optimal electron density contribution from the clusters to the bound intermediates, specifically oxygen in our case.[30] The computed slopes of E_{*O} *vs.* E_{*OH} and E_{*OH} *vs.* E_{*OOH} varied from the expected values of 0.5 and 1.0, reflecting a decreased electron contribution to the bound oxygen atom (Fig. 2).[30] This also signifies the inadequacy of the effective medium theorem for small clusters in generalizing E_{ads} across subnano clusters.[18] These results demonstrate the potential of size and transition metal variation to modify the scaling relationship and reshape the activity volcano plots in the subnanometer regime.

2.3. Evaluating the OER/ORR electrocatalytic performance

Next, we derived the OER and ORR reaction mechanism to screen for active electrocatalysts by simulating a four-electron reaction at 0 V (without any external potential) and 1.23 V (equilibrium potential) in an acidic medium.[31] The elementary steps of both reactions are as follows:

In an acidic medium, the OER is considered a four-step process as follows:

$$* + H_2O(l) \rightarrow OH^* + (H^+ + e^-) \quad (\Delta R_1)$$

$$OH^* \rightarrow O^* + (H^+ + e^-) \quad (\Delta R_2)$$

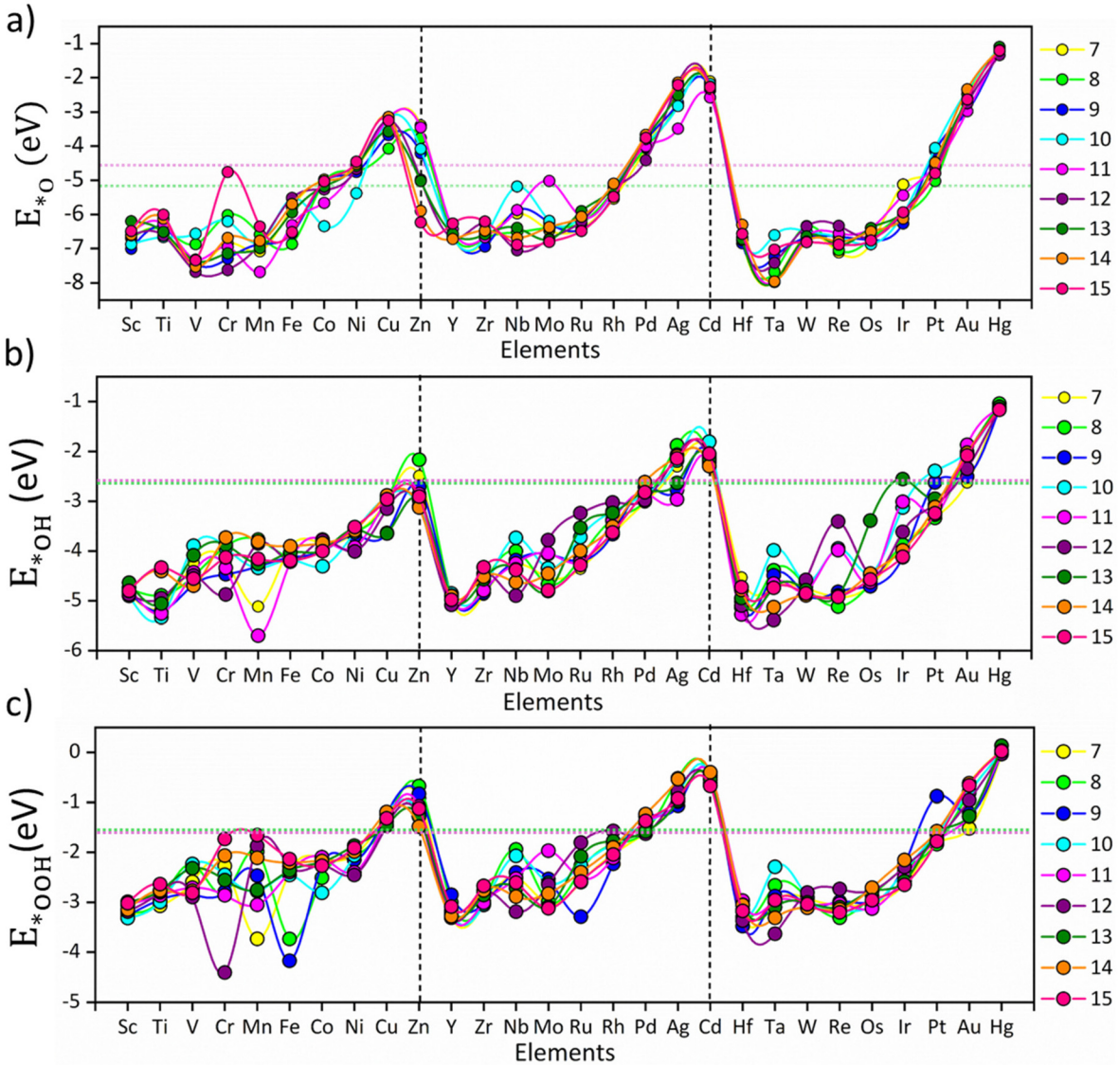

Fig. 1 Adsorption energy trends of *O, *OH and *OOH intermediates: (a) E_{*O}, (b) E_{*OH} and (c) E_{*OOH} on the investigated TM_n subnano clusters, represented by circles. The colors represent different-sized subnano clusters (n = 7–15), as denoted in the legends. The vertical lines separate the 3d, 4d, and 5d transition metals, and the solid lines connecting the different dot markers are guides for the eye. The pink and green dotted horizontal lines represent the adsorption energy of intermediates on the Pt (111) surface and Pt_{79} nanoclusters, respectively, for comparison with the bulk surfaces.

$$O^* + H_2O(l) \rightarrow OOH^* + (H^+ + e^-) \quad (\Delta R_3)$$

$$OOH^* \rightarrow O_2(g) + (H^+ + e^-) + * \quad (\Delta R_4)$$

And the $4e^-$ ORR is the reverse reaction of the OER with four-step as follows:

$$O_2\ (g) + (H^+ + e^-) + * \rightarrow OOH^* \quad (\Delta R_5)$$

$$OOH^* + (H^+ + e^-) \rightarrow O^* + H_2O(l) \quad (\Delta R_6)$$

$$O^* + (H^+ + e^-) \rightarrow OH^* \quad (\Delta R_7)$$

$$OH^* + (H^+ + e^-) \rightarrow H_2O(l) + * \quad (\Delta R_8)$$

To compare the catalytic activity of the TM_n subnano clusters, the overpotential values (η) of the rate-determining step (RDS) at 1.23 V were utilized to evaluate the OER/ORR performance of the catalyst,[31] as depicted in Fig. 3. The theoretical overpotential at 1.23 V is calculated by the equation:

$$\eta_{OER} = \frac{\max(\Delta R_1, \Delta R_2, \Delta R_3, \Delta R_4)}{e}$$

$$\eta_{ORR} = \frac{\max(\Delta R_5, \Delta R_6, \Delta R_7, \Delta R_8)}{e}$$

The two-electron pathway leading to peroxide formation was not investigated because of the unstable adsorption

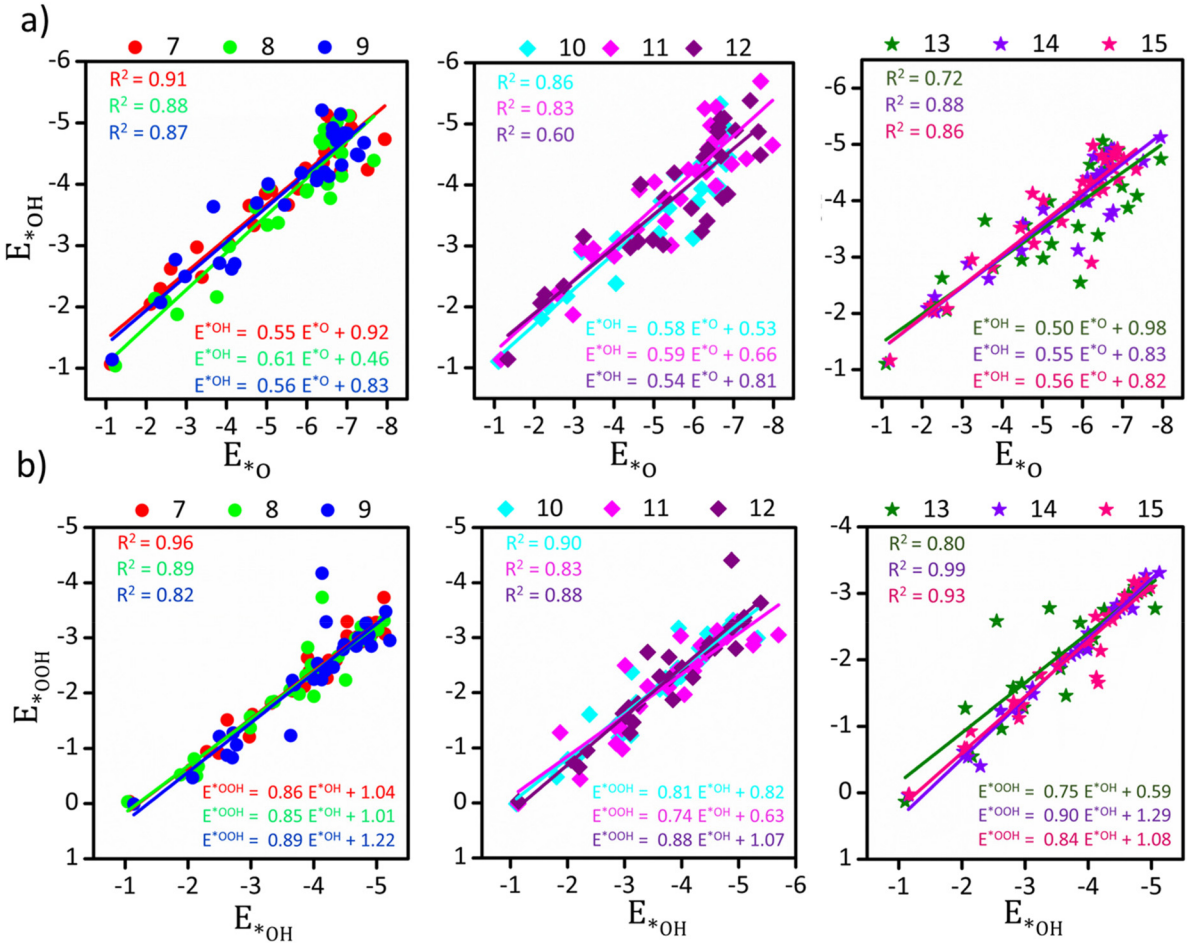

Fig. 2 Scaling relationship between (a) E_{*O} *vs.* E_{*OH} and (b) E_{*OH} *vs.* E_{*OOH} for different-sized TM_n subnano clusters. The sizes are represented in colors on the top panel. The coefficient of determination (R^2) and linear fit equations representing the slope of the best-fitted line corresponding to each size range are shown in the plots.

(breaking) of the H_2O_2 intermediates on subnano clusters, as reported in our previous investigations.[19,28] The OER/ORR activity with respect to the size and element in the subnanometer regime is summarized in Fig. 3.

As depicted in Fig. 3, catalytic activity varies non-monotonically with size and elemental composition in the subnanometer regime. For the OER, Au_{11}, Pd_{13}, and Ag_8 emerged as active electrocatalysts with lower η_{OER} values of 0.22, 0.34, and 0.43 V, respectively, with the RDS involving *OH → *O (ΔR_2) formation (Fig. 3, Fig. S2†). These η_{OER} values are lower (or comparable) to traditional active OER catalysts, such as RuO_2 (η_{OER} = 0.42 V) and IrO_2 (η_{OER} = 0.56 V).[32] Interestingly, Au_{11} also exhibits superior OER activity compared to previously theoretically reported carbon-based single-atom catalysts like N/C-coordinated graphene (Co-doped), C_2N (Ni-doped), C_3N_4 (Ni-doped), graphdiyne (Co-doped), covalent organic framework (Cu-doped), and metal–organic framework (Co-doped), which show η_{OER} values of 0.46 V, 0.34 V, 0.96 V, 0.64 V, 0.69 V, and 0.29 V, respectively.[33] In contrast, Zn_{15}, V_{13}, and Ta_8 are identified as inactive OER electrocatalysts with significantly higher η_{OER} values of 3.22 V, 3.16 V, and 3.13 V respectively, with the RDS of *O → *OOH (ΔR_3) formation. For the ORR, Au_{11}, Pt_{10}, and Au_9 have emerged as active electrocatalysts with lower η_{ORR} values of 0.21, 0.35, and 0.45 V, respectively. In contrast, Mn_{11}, Ta_{12}, and Ti_{10} are categorized as the poor electrocatalysts with higher η_{ORR} values of 3.65 V, 3.33 V, and 3.28 V, respectively. For most electrocatalysts, the RDS for the ORR involves of *OH → H_2O(l) (ΔR_8) formation. However, for Ag_8, Ag_{10}, Au_{12}, and Au_{15}, the RDS is O_2(g) → *OOH formation (ΔR_5). Compared to an ideal system such as Pt (111) surface with η_{ORR} = 0.45 V,[34] these catalysts exhibit enhanced ORR activity. Conversely, for Au_{13}, Au_7, and Au_{11}, the RDS involves the *OOH → *O + H_2O(l) (ΔR_6) formation, while for Ir_{11}, Ru_{12}, Pt_{10} and Ir_{13}, the RDS constitutes the *O → *OH (ΔR_7) formation. Interestingly, we observe size-dependent reshaping of the OER/ORR activity volcano in the subnanometer regime, where the apex of the plot shifts from benchmarked systems such as RuO_2 and Pt (111) surface to the Au_9, Au_{11}, and Au_8 subnano clusters. Apart from Au_{11} clusters, Pd_{13} and Pt_{10} clusters have also emerged as active catalysts for OER and ORR activity, respectively. For each active OER/ORR electrocatalysts in the subnanometer regime, the adsorption energy for each

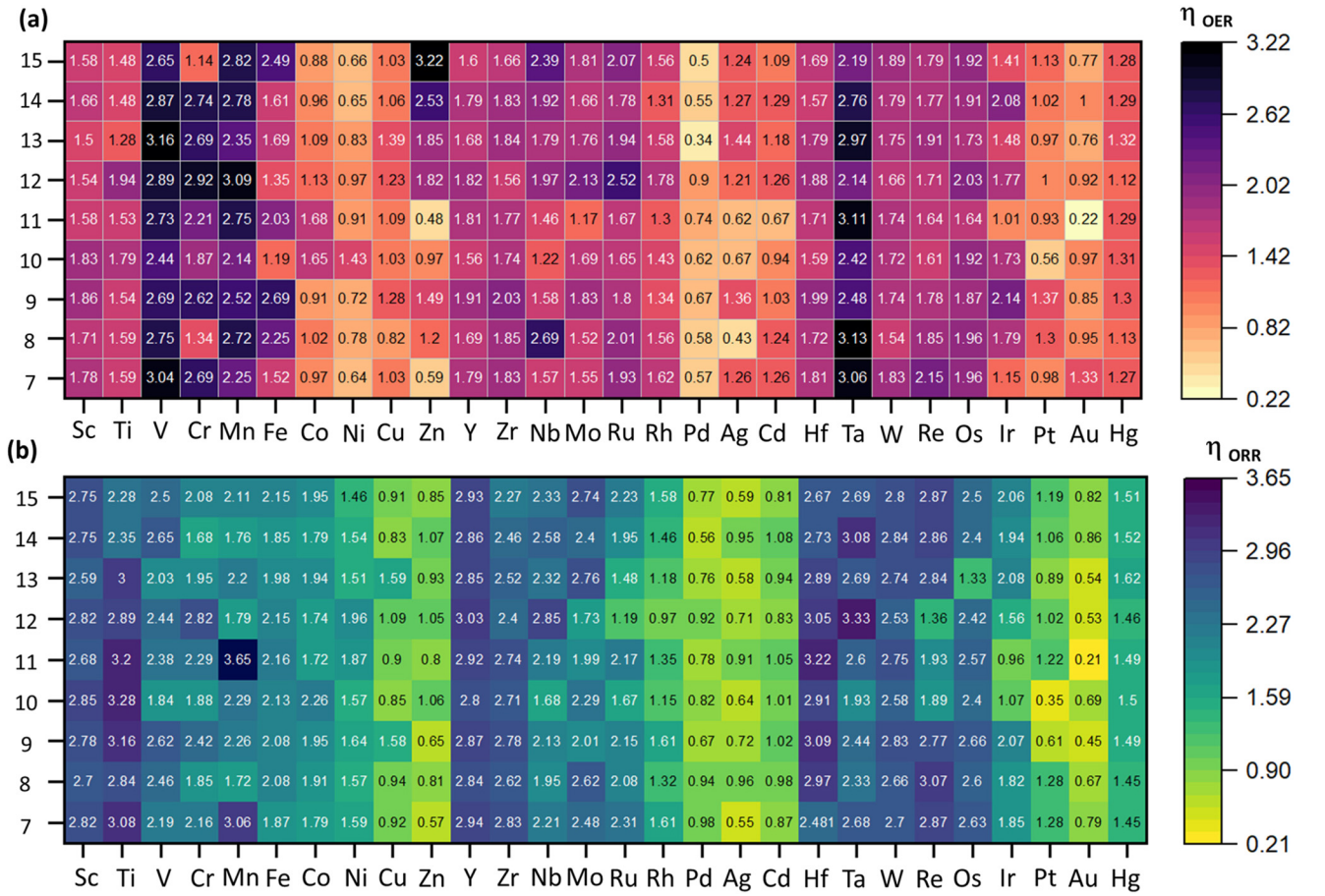

Fig. 3 Activity heap maps for (a) OER, and (b) ORR activities across different catalysts. The numeric values correspond to the overpotential values (η) of the rate-determining step (RDS) calculated at 1.23 V to measure the catalytic activity. The scale on the right represents the range of values, where light orange and yellow represent higher activity, and the dark color represents lower activity.

intermediate lies within $-4.10 < E_{ads} < -1.23$ eV range (Table 1). This range of E_{ads} could potentially be utilized to extract subnano clusters exhibiting optimal adsorption energetics and higher activity in the subnanometer regime.

From Fig. 3, it is evident that TM_n clusters with v^1–v^5 electronic configurations exhibited higher η_{OER}/η_{ORR} values, rendering them unsuitable for both reactions in the subnanometer regime. Interestingly, compared to the early transition metal subnano clusters, the late transition metal subnano with v^8–v^{10} configurations exhibited a significant decrease in η_{OER} and η_{ORR} values (Fig. 3), making them suitable for fuel cell electrocatalysis.

Table 1 Adsorption energies (E_{ads}) of *O, *OH, and *OOH for the OER/ORR active and inactive electrocatalysts. Each catalyst's overpotential values (η) were calculated at 1.23 V for the rate-determining step (RDS)

Reaction	Activity	Catalysts	*O (eV)	*OH (eV)	*OOH (eV)	Overpotential values (η)
OER	Active	Au_{11}	−2.97	−1.87	−1.28	0.22
		Pd_{13}	−3.79	−2.81	−1.58	0.34
		Ag_8	−2.77	−1.88	−0.52	0.43
	Inactive	Zn_{15}	−6.23	−2.90	−1.12	3.22
		V_{13}	−7.36	−4.08	−2.32	3.16
		Ta_8	−7.67	−4.39	−2.66	3.13
ORR	Active	Au_{11}	−2.97	−1.87	−1.28	0.21
		Pt_{10}	−4.05	−2.39	−1.61	0.35
		Au_9	−2.97	−2.49	−1.22	0.45
	Inactive	Mn_{11}	−7.68	−5.69	−3.05	3.65
		Ta_{12}	−7.41	−5.38	−3.63	3.33
		Ti_{10}	−6.66	−5.33	−2.99	3.28

2.4. Screening of potential bifunctional OER/ORR subnano catalysts

In fuel cells, OER corresponds to the charging process, while the ORR is associated with the battery discharge process. Therefore, to screen bifunctional subnano catalysts that facilitate both the OER and ORR in the subnanometer regime, we computed a widely accepted descriptor $\eta_{Bi} = \eta_{OER} + \eta_{ORR}$,[35] where catalysts with lower η_{Bi} exhibit high electrocatalytic performance, as shown in Fig. 4. The bifunctional catalytic activity demonstrates nonlinear variation with size and elemental composition, with subnano clusters featuring v^9/v^{10} configuration exhibit lower η_{Bi} values. Conversely, subnano clusters with v^1–v^5 configuration exhibit significantly higher η_{Bi} values, indicating their inactivity as electrocatalysts in the subnanometer regime. Interestingly, Au_{11} emerged as the best bifunctional electrocatalysts with a low η_{Bi} = 0.43 V. This value is even lower than the 1.01 V of Ru/C,[36] which has been reported as the best bifunctional electrocatalyst. In contrast, Mn_{11} emerged as an inactive bifunctional electrocatalysts with a high η_{Bi} = 6.40 V.

2.5. Descriptors for bifunctional catalytic activity

Furthermore, to screen the potential bifunctional electrocatalysts and gain deeper insights into the electronic descriptors affecting their activity, we categorized the bifunctional catalysts into three clusters: active, medium active, and inactive catalysts based on the η ranges listed in Table 2. The higher and lower limits of the η_{OER} and η_{ORR} values were approximated based on the results of previous literature.[4,19,28,35–41]

Furthermore, to elucidate the origin of bifunctional activities in our investigation, it is crucial to evaluate the descriptors that significantly influence OER and ORR activities. Therefore, to encode the electronic characteristics of TM_n in our investigation, we extracted descriptors into three different categories: (1) elemental, (2) electronic, and (3) d-band specific features, as tabulated in Table 3. The elemental features provide a physical description of the TM. However, the electronic descriptors pertain to the electron acceptance/donation capability of different TM. Previous investigations have evidenced the d-band center (ε_d) as an effective descriptor to relate the catalysts' electronic structure to the intermediates' adsorption strength.[24,42–44] However, considering the vast chemical space in our investigations, it becomes prohibitively expensive to extract ε_d with self-consistent quantum calculations. To circumvent this, we attempted to encode the elemental-specific numeric values of the d-band characteristics from the Solid State Table (relative to Cu) provided for the surfaces.[45] Each feature regulates the inherent d-band electronic characteristics, which can be substituted without expensive DFT calcu-

Table 2 Range for OER and ORR active electrocatalysts for screening active bifunctional active catalysts

Cluster	OER range (V)	ORR range (V)	Instances
Cluster 1	$0.00 < \eta < 0.40$	$0.00 < \eta < 0.45$	1
Cluster 2	$0.45 < \eta < 0.80$	$0.45 < \eta < 0.80$	10
Cluster 3	$0.80 < \eta$	$0.80 < \eta$	251

Table 3 List of descriptors including elemental, electronic, and d-band specific features

Category	Features	Symbol
Elemental	Sum of atomic weight	$\sum A$
	Sum of covalent radii	$\sum r_c$
	Bulk Wigner Seitz radii	S_{BW}
	Sum of bulk Wigner Seitz radii	$\sum S_{BW}$
Electronic	d orbital energy	E_d
	Sum of d orbital energy	$\sum E_d$
	Sum of d electrons	$\sum d_n$
	Sum of electronegativity	$\sum \chi_n$
	First ionization potential (eV)	IP_1
d-Band specific	Coupling matrix	V_{ad}^2
	Idealized d band filling (size dependent)	I_{df}
	Size-dependent d-band center	ε_d

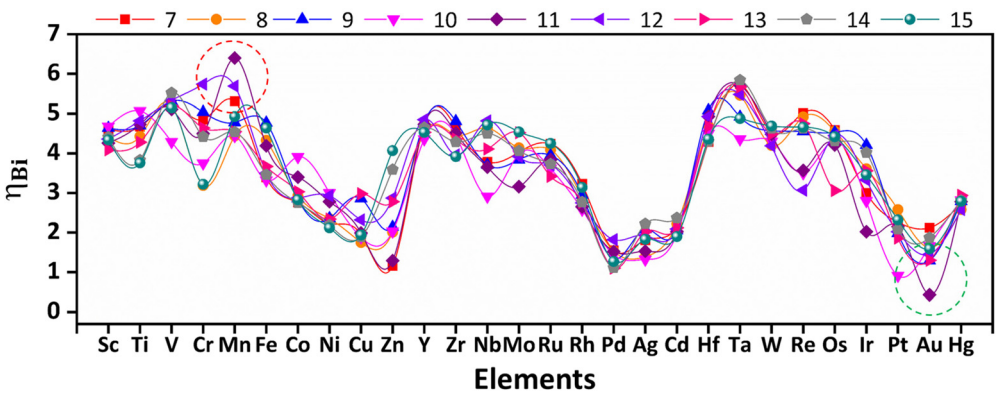

Fig. 4 Trends of bifunctional activity across 3d, 4d, and 5d TM_n subnano clusters, computed as $\eta_{Bi} = \eta_{OER} + \eta_{ORR}$. The solid lines connecting different dot markers are guides for the eye, representing different sizes and elements. The colors represent different-sized subnano clusters (n = 7–15), as denoted in the legends. The active and inactive bifunctional catalysts are enclosed within green and red circles, respectively.

lations. Note that the individual features (S_{BW}, E_d, IP_1, $V_{ad}{}^2$, I_{df}, and ε_d) correlates with the single metal atoms of the subnano clusters; however, the summation features ($\sum A$, $\sum r_c$, $\sum S_{BW}$, $\sum E_d$, $\sum d_n$, and $\sum \chi_n$) are included to differentiate between the different-sized metal clusters.

We analyzed the correlation plots of OER/ORR catalysts after categorizing them into active, medium active, and inactive catalysts, as shown in Fig. 5a. The linear correlation between the feature-feature and feature-OER/ORR activity can be assessed using the Pearson correlation coefficient (PCC).[46,47] Most pairwise feature distributions, as shown in Fig. 5b, exhibited low correlation ($|PCC| < 0.8$), indicating their independent influence on catalytic activity, and were allowed to coexist. Note that features such as $\sum A$, $\sum r_c$, E_d, and $\sum E_d$ exhibited a significantly low correlation with the OER and ORR activity ($|PCC| \sim 0$), suggesting they do not predict the changes in OER and ORR activity. Consequently, we removed highly correlated features that exhibited a low impact on ORR/OER activity from our final dataset to avoid data redundancy. The final list of features and their correlations is provided in Table 4. Overall, the OER and ORR activities of the subnano clusters can be described as follows:

$$\eta_{OER/ORR} = f(S_{BW}, \sum S_{BW}, \sum E_d, \sum d_n, \sum \chi_n, IP_1, I_{df}, \varepsilon_d) \quad (2)$$

Following the feature selection process, we employed the Random Forest regression (RFR) to assess the feature importance towards OER and ORR activity, as shown in Fig. 5c and d. The RFR method is based on an ensemble of decision trees from which the prediction of a continuous variable is provided as the average of the prediction of all trees.[48] Most importantly, the RFR model evaluates the significance of descriptors in the model by sequentially replacing each descriptor with random noise and observing the resulting decline in model performance, which is measured by the change in the mean-square-error (MSE) for the out-of-bag (OOB) validation data when the descriptor is replaced.[48] Interestingly, I_{df} demonstrates the highest and equal contribution towards the OER and ORR activities, suggesting its

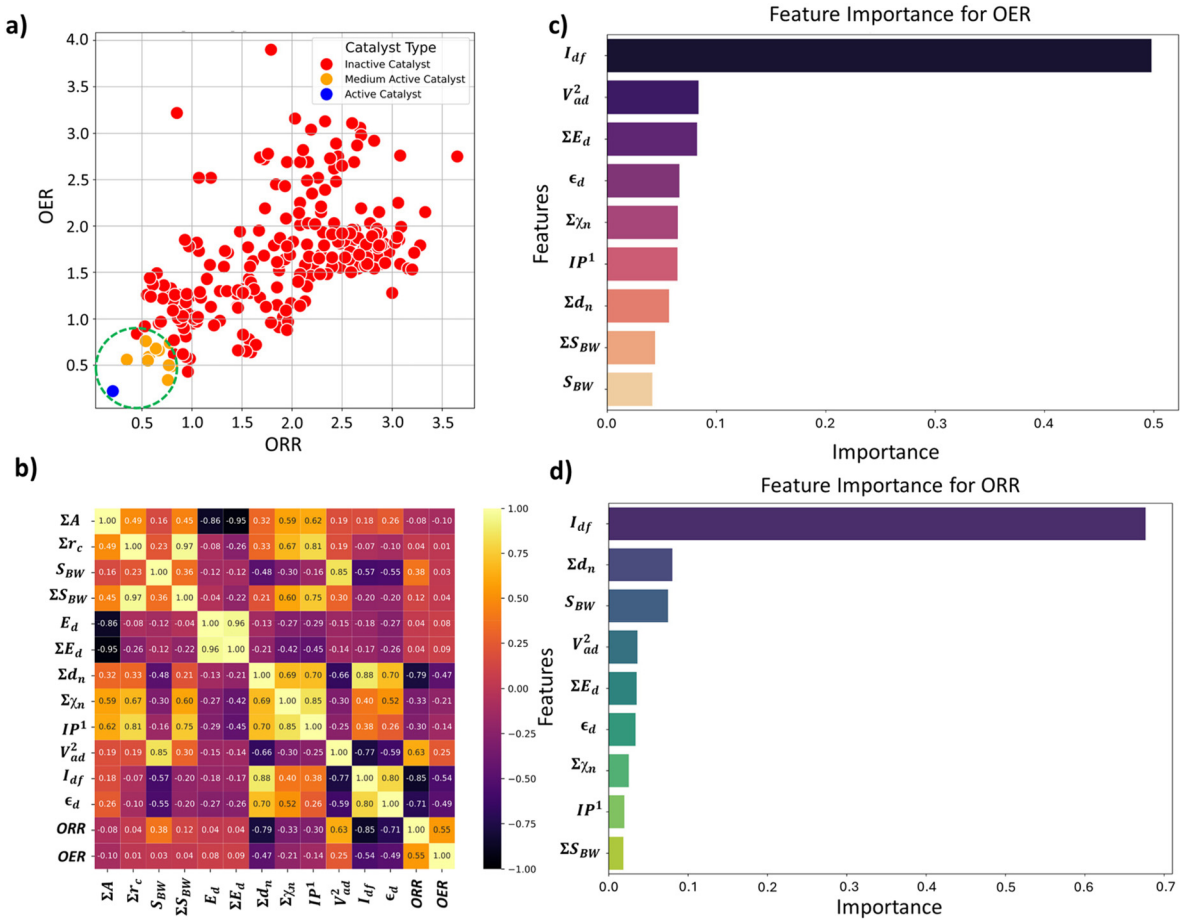

Fig. 5 (a) Distribution of OER and ORR overpotential values (η) to screen active bifunctional catalysts. (b) Feature-feature and feature-output correlation matrix displaying Pearson's correlation coefficient (PCC) for OER and ORR datasets. The scale on the right represents the range of correlation, where the yellow and black colors represent perfect positive and negative correlations, respectively. Feature importance for (c) OER and (d) ORR activity.

Table 4 List of descriptors including elemental, electronic, and d-band specific features exhibiting low correlations

Features	Symbol	Pearson correlation coefficient
Bulk Wigner Seitz radii	S_{BW}	
Sum of bulk Wigner Seitz radii	$\sum S_{BW}$	
Sum of d orbital energy	$\sum E_d$	
Sum of d electrons	$\sum d_n$	
Sum of electronegativity	$\sum \chi_n$	
First ionization potential (eV)	IP_1	
Coupling matrix	$V_{ad}{}^2$	
Idealized d band filling (size dependent)	I_{df}	
Size-dependent d-band center	ϵ_d	

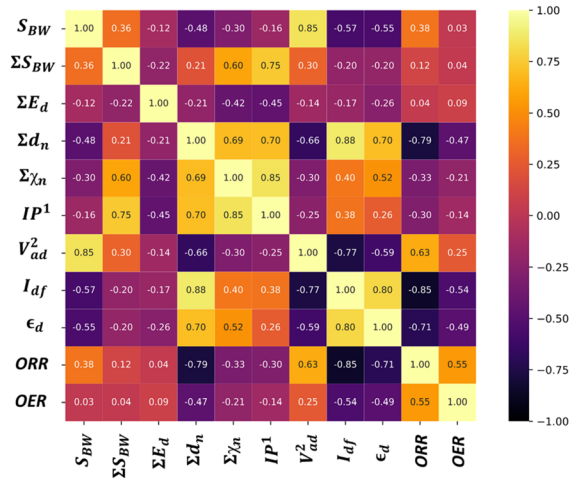

effectiveness in identifying bifunctional active catalysts in the subnanometer regime. However, the contributions of the other features are low and offset each other, reflecting their unidirectional utilization towards either OER or ORR activity. Note that the d-band model developed by Hammer and Nørskov systematically correlates the perturbations in the adsorbate to the position of the ε_d relative to the Fermi level (E_f), is limited to pure transition metals and certain alloys; however, it fails to describe interactions on more complex metal surfaces adequately.[49–52] In contrast, the I_{df} outperformed the ε_d at the subnanometer regime, effectively capturing the elemental-specific d-state contributions of the unique local coordination environment while accounting for the perturbations introduced by the complex chemical environment of subnano clusters. Upon closer examination of the active bifunctional catalyst Au_{11}, a higher I_{df} value (1.0) resulted in weak coupling between the metal and intermediates, driving the E_{ads} values of intermediates towards lower levels, leading to optimum binding energetics (Fig. S3†). In contrast, lower I_{df} values (0.6) observed for inactive bifunctional catalysts, such as Mn_{11}, resulted in stronger binding, which ultimately increased the η values. Similar trends were observed for high values of ε_d, which reduced binding strength and consequently lowered η values (Fig. S3†). The feature $\sum S_{BW}$ consistently appeared at the bottom of the plots with its minimal impact, demonstrating its lowest contribution to the OER and ORR activities. For enhanced OER/ORR bifunctional activity, catalysts at the apex of activity volcano plots should exhibit near-optimal adsorption energetics for each reaction intermediate. Similarly, Au_{11} bifunctional catalyst achieves optimal adsorption energies for *O, *OH, and *OOH within the range of -4.92 eV $< E_{ads} < -1.23$ eV, suggesting weaker binding than the Pt (111) surface. Additionally, to understand electronic structures during the OER/ORR intermediate adsorption on Au_{11} subnano clusters, we performed a partial density of states (PDOS) analysis, represented in Fig. 6. The narrow distribution of 5d states near the Fermi level (E_f) indicates weaker coupling between Au (5d) and O (2p) states, further driving the E_{ads} values towards the optimal range. Overall, our study emphasizes the significant contribution of idealized d-band filling while encoding the complex relations of OER/ORR activities at the subnanometer regime, presenting a new pathway for designing efficient bifunctional electrocatalysts.

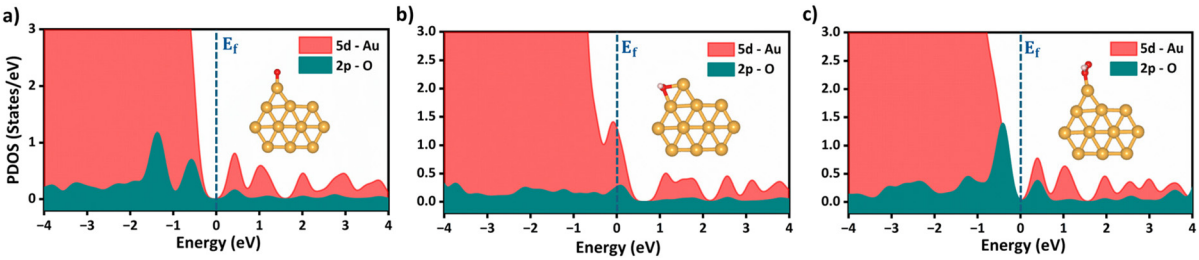

Fig. 6 Partial density of states (PDOS) for (a) *O, (b) *OH and (c) *OOH adsorbed Au_{11} bifunctional catalysts. The Fermi level at 0.00 eV is represented as (E_f). The inset represents the stable adsorption configurations of the reaction intermediates onto Au_{11} subnanoclusters.

3. Conclusions

In summary, we demonstrate a breaking of conventions for OER and ORR activity across 3d, 4d, and 5d transition metal TM_n subnano clusters. Owing to the fluxionality and non-monotonic catalytic activity at the subnanometer regime, we observe a shift in the apex of the activity volcano from Pt(111)/IrO_2 to Au_{11} clusters. Compared to early transition metal clusters (with ν^1–ν^5 configurations), the late transition metal clusters (with ν^8–ν^{10} configurations) exhibited significantly reduced overpotential values for OER/ORR activity, highlighting their potential in the theoretical and experimental screening of bifunctional catalysts. Interestingly, Au_{11} emerged as a top bifunctional electrocatalyst exhibiting low bifunctional overpotential values (η_{Bi}) of 0.43 V. Further, impinging on the non-*ab initio* electronic descriptors, we demonstrate the significant contribution of the idealized d-band filling (I_{df}) feature towards the bifunctional activity at the subnanometer regime. Additionally, our observations also align with the d-band theory where higher values of I_{df} and d-band center (ε_d) lead to optimal reaction energetics, thereby reducing the η_{Bi} values due to weak intermediate binding strengths. Thus, our work correlates the electronic descriptors of the subnano clusters with their OER and ORR activities, opening new avenues for effectively designing and screening efficient bifunctional cluster catalysts.

Data availability

The data supporting the findings of this study can be found at **https://github.com/Rahul2101131005/Bifunctional-Active-Subnano-Clusters-08-07-2024-.git**.

Conflicts of interest

There are no conflicts to declare.

Acknowledgements

We acknowledge IIT Indore for providing the lab/computational facilities and CSIR (01(3046)/21/EMR-II), DST-SERB (CRG/2022/000836) and BRNS (2023-BRNS/12356) projects for funding. R.K.S. thanks UGC for the research fellowship, and H.M. thanks PMRF for the research fellowship.

References

1 N. S. Lewis, *Science*, 2016, **351**(6271), aad1920.
2 Z. W. She, J. Kibsgaard, C. F. Dickens, I. Chorkendorff, J. K. Nørskov and T. F. Jaramillo, *Science*, 2017, **355**(6321), eaad4998.
3 S. S. Shinde, C. H. Lee, J. Y. Jung, N. K. Wagh, S. H. Kim, D. H. Kim, C. Lin, S. U. Lee and J. H. Lee, *Energy Environ. Sci.*, 2019, **12**(2), 727–738.
4 Z. F. Huang, J. Wang, Y. Peng, C. Y. Jung, A. Fisher and X. Wang, *Adv. Energy Mater.*, 2017, **7**(23), 1700544.
5 Z. Shi, J. Li, Y. Wang, S. Liu, J. Zhu, J. Yang, X. Wang, J. Ni, Z. Jiang, L. Zhang, Y. Wang, C. Liu, W. Xing and J. Ge, *Nat. Commun.*, 2023, **14**(1), 843.
6 X. Cui, P. Ren, D. Deng, J. Deng and X. Bao, *Energy Environ. Sci.*, 2016, **9**(1), 123–129.
7 L. Bai, C. S. Hsu, D. T. L. Alexander, H. M. Chen and X. Hu, *Nat. Energy*, 2021, **6**(11), 1054–1066.
8 Y. Wang, D. Wang and Y. Li, *SmartMat*, 2021, **2**(1), 56–75.
9 L. Zhang, L. T. Roling, X. Wang, M. Vara, M. Chi, J. Liu, S. Il Choi, J. Park, J. A. Herron, Z. Xie, M. Mavrikakis and Y. Xia, *Science*, 2015, **349**(6246), 412–416.
10 R. Gao, J. Wang, Z. F. Huang, R. Zhang, W. Wang, L. Pan, J. Zhang, W. Zhu, X. Zhang, C. Shi, J. Lim and J. J. Zou, *Nat. Energy*, 2021, **6**(6), 614–623.
11 Z. Liu, Y. Ma, W. Gu, C. Yuan and F. Teng, *J. Phys. Chem. Solids*, 2020, **147**, 109578.
12 Y. J. Wang, N. Zhao, B. Fang, H. Li, X. T. Bi and H. Wang, *Chem. Rev.*, 2015, **115**(9), 3433–3467.
13 Q. Fu and C. Draxl, *Phys. Rev. Lett.*, 2019, **122**(4), 046101.
14 Z. Fu, B. Yang and R. Wu, *Phys. Rev. Lett.*, 2020, **125**(15), 156001.
15 B. Jiang, F. Zhang, Y. Wang, X. Xue, J. Shi, X. Zhao, L. Zhang, R. Pang, X. Ren, S. Li and Z. Zhang, *Phys. Rev. B*, 2023, **107**(20), 205421.
16 E. J. Peterson, A. T. DeLaRiva, S. Lin, R. S. Johnson, H. Guo, J. T. Miller, J. H. Kwak, C. H. F. Peden, B. Kiefer, L. F. Allard, F. H. Ribeiro and A. K. Datye, *Nat. Commun.*, 2014, **5**(1), 4885.
17 H. Zhai and A. N. Alexandrova, *ACS Catal.*, 2017, **7**(3), 1905–1911.
18 B. Zandkarimi and A. N. Alexandrova, *J. Phys. Chem. Lett.*, 2019, **10**(3), 460–467.
19 R. K. Sharma, H. Minhas and B. Pathak, *J. Phys. Chem. C*, 2024, **128**(18), 7504–7517.
20 X. Shi, Y. Li, S. Zhang, R. Hu, S. Gao, P. Jin, J. Shang and J. Shui, *Nano Res.*, 2023, **16**(5), 8042–8050.
21 Z. Zhang, B. Zandkarimi, J. Munarriz, C. E. Dickerson and A. N. Alexandrova, *ChemCatChem*, 2022, **14**(15), e202200345.
22 A. S. Chaves, M. J. Piotrowski and J. L. F. Da Silva, *Phys. Chem. Chem. Phys.*, 2017, **19**(23), 15484–15502.
23 L. Zhang, X. Guo, S. Zhang and S. Huang, *J. Mater. Chem. A*, 2022, **10**(21), 11600–11612.
24 M. O. J. Jäger, Y. S. Ranawat, F. F. Canova, E. V. Morooka and A. S. Foster, *ACS Comb. Sci.*, 2020, **22**(12), 768–781.
25 A. S. Nair and B. Pathak, *J. Phys. Chem. C*, 2019, **123**(6), 3634–3644.
26 T. Bligaard, J. K. Nørskov, S. Dahl, J. Matthiesen, C. H. Christensen and J. Sehested, *J. Catal.*, 2004, **224**(1), 206–217.

27 P. Ferrin, D. Simonetti, S. Kandoi, E. Kunkes, J. A. Dumesic, J. K. Nørskov and M. Mavrikakis, *J. Am. Chem. Soc.*, 2009, **131**(16), 5809–5815.
28 R. K. Sharma, A. S. Nair, N. Bharadwaj, D. Roy and B. Pathak, *J. Phys. Chem. C*, 2023, **127**(1), 127–228.
29 J. P. Perdew, J. A. Chevary, S. H. Vosko, K. A. Jackson, M. R. Pederson, D. J. Singh and C. Fiolhais, *Phys. Rev. B: Condens. Matter Mater. Phys.*, 1992, **46**(11), 6671.
30 M. M. Montemore and J. W. Medlin, *Catal. Sci. Technol.*, 2014, **4**(11), 3748–3761.
31 J. K. Nørskov, J. Rossmeisl, A. Logadottir, L. Lindqvist, J. R. Kitchin, T. Bligaard and H. Jónsson, *J. Phys. Chem. B*, 2004, **108**(46), 17886–17892.
32 I. C. Man, H. Y. Su, F. Calle-Vallejo, H. A. Hansen, J. I. Martínez, N. G. Inoglu, J. Kitchin, T. F. Jaramillo, J. K. Nørskov and J. Rossmeisl, *ChemCatChem*, 2011, **3**(7), 1159–1165.
33 Y. Wang, X. Huang, H. Fu and J. Shang, *J. Mater. Chem. A*, 2022, **10**(45), 24362–24372.
34 J. Zhang, Z. Zhao, Z. Xia and L. Dai, *Nat. Nanotechnol.*, 2015, **10**(5), 444–452.
35 B. Wei, Z. Fu, D. Legut, T. C. Germann, S. Du, H. Zhang, J. S. Francisco and R. Zhang, *Adv. Mater.*, 2021, **33**(40), 2102595.
36 M. Prabu, K. Ketpang and S. Shanmugam, *Nanoscale*, 2014, **6**(6), 3173–3181.
37 A. Kulkarni, S. Siahrostami, A. Patel and J. K. Nørskov, *Chem. Rev.*, 2018, **118**(5), 2302–2312.
38 T. Zhang, B. Zhang, Q. Peng, J. Zhou and Z. Sun, *J. Mater. Chem. A*, 2021, **9**(1), 433–441.
39 H. Niu, X. Wan, X. Wang, C. Shao, J. Robertson, Z. Zhang and Y. Guo, *ACS Sustainable Chem. Eng.*, 2021, **9**(9), 3509–3599.
40 A. S. Nair, A. Mahata and B. Pathak, *ACS Appl. Energy Mater.*, 2018, **1**(8), 3890–3899.
41 A. S. Nair, A. Anoop, R. Ahuja and B. Pathak, *J. Comput. Chem.*, 2021, **42**(27), 1944–1958.
42 B. Hammer and J. K. Nørskov, *Adv. Catal.*, 2000, **45**, 71–129.
43 H. Xin and S. Linic, *J. Chem. Phys.*, 2010, **132**(22), 221101.
44 A. Vojvodic, J. K. Nørskov and F. Abild-Pedersen, *Top. Catal.*, 2014, **57**, 25–32.
45 A. Ruban, B. Hammer, P. Stoltze, H. L. Skriver and J. K. Nørskov, *J. Mol. Catal. A: Chem.*, 1997, **155**(3), 421–429.
46 B. Li, P. Zhang, S. Liang and G. Ren, in *International Conference on Signal Processing Proceedings*, ICSP, 2008.
47 N. N. Wang, J. Dong, Y. H. Deng, M. F. Zhu, M. Wen, Z. J. Yao, A. P. Lu, J. B. Wang and D. S. Cao, *J. Chem. Inf. Model.*, 2016, **56**(4), 763–773.
48 D. S. Palmer, N. M. O'Boyle, R. C. Glen and J. B. O. Mitchell, *J. Chem. Inf. Model.*, 2007, **47**(1), 150–158.
49 S. Saini, J. Halldin Stenlid, S. Deo, P. N. Plessow and F. Abild-Pedersen, *ACS Catal.*, 2024, **14**(2), 874–885.
50 S. Saini, J. Halldin Stenlid and F. Abild-Pedersen, *npj Comput. Mater.*, 2022, **8**, 163.
51 W. Gao, Y. Chen, B. Li, S.-P. Liu, X. Liu and Q. Jiang, *Nat. Commun.*, 2020, **11**, 1196.
52 B. Li, X. Li and W. Gao, *J. Mater. Chem. A*, 2022, **10**(12), 6731–6739.